Supplementary Material for

"Flavour-selective localization in interacting lattice fermions via SU(N) symmetry breaking"

D. Tusi, L. Franchi, L. F. Livi, K. Baumann, D. Benedicto Orenes, L. Del Re, R. E. Barfknecht
T. Zhou, M. Inguscio, G. Cappellini, M. Capone, J. Catani, L. Fallani

S.I. MEASUREMENT OF DOUBLE OCCUPANCIES

We measure double occupancies (doublons) in the 3D lattice exploiting a one-color photoassociation (PA) process which transfers the atoms in doubly-occupied lattice sites into highly excited molecular states[19]. The photoassociated atoms are rapidly lost from the lattice due to the fast decay of the molecular states, leaving a sample consisting only of singly-occupied sites. The number of double occupancies is thus inferred by first measuring the total number of atoms in the sample and then subtracting the number of atoms in singly occupied lattice sites remaining after the PA pulse. For the regime of atom number considered in this work we expect the number of triply-occupied sites to be negligible.

Our measurement procedure starts with a rapid freeze of the atomic density distribution that we realize increasing the lattice depth up to $V_0 = 25E_{rec}$ ($E_{rec} = h^2/8md^2$, where h is the Planck constant, m the atomic mass and d the lattice spacing) in a time 1.5 ms. At the final lattice depth tunnelling between lattice sites is completely negligible. Two different schemes are then employed for the PA excitation depending on the specific measurement that we want to perform.

In order to measure the total number of doublons independently on their spin composition (results of Fig. 2 of the main text), a 5 ms long, σ^- polarized PA pulse is shone on the atomic sample with an intensity $I_{PA} = 90$ mW/mm^2. The PA pulse excites a molecular line that is 796.2 MHz red-detuned with respect to the $^1S_0(F = 5/2) \rightarrow {}^3P_1(F = 7/2)$ atomic transition[16]. During the process, atoms are subjected to a low magnetic field $B = 3$ G which defines a quantization axis for the spin, but is low enough not to unveil the Zeeman substructure of the molecular line, as it is shown in the spectrum reported in Fig. S1a.

In the presence of a higher external magnetic field, the PA transition frequency is shifted accordingly to the projection M_T of the molecular total angular momentum on the quantization axis[S1]. M_T is a quantum number conserved during the PA process, with a value given by the relation $M_T = m_1 + m_2 + \sigma$, where $m_{1,2}$ are the nuclear spin projections of the the two atoms composing the molecule and $\sigma = -1$ is the angular momentum transferred by the PA photon. As long as the sum $m_1 + m_2$ unambiguously characterizes an atomic pair, the molecular Zeeman substructure can thus be employed as a tool to distinguish between doublons with different spin flavours

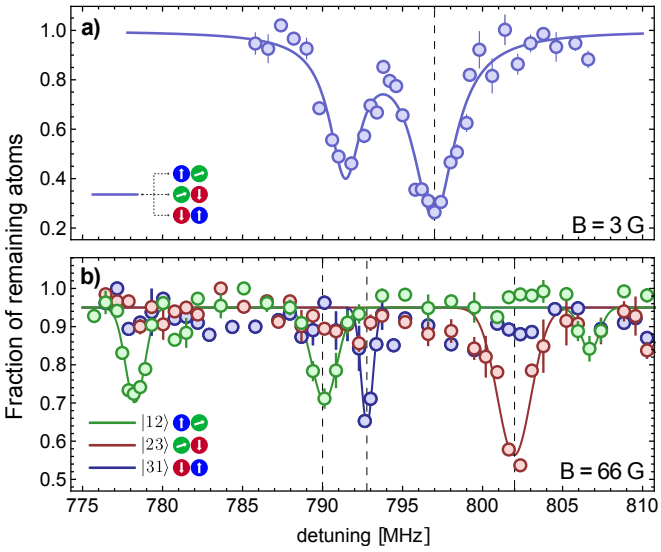

FIG. S1. **Detection of double occupancies.** Photoassociation spectroscopy on an SU(3) atomic sample (a) and on different SU(2) mixtures (b). The plots report the number of atoms remaining in the sample after a 5 ms long PA pulse at low laser intensity (unsaturated regime).

Taking this into consideration, in order to detect only doublons with a particular spin composition $\{m_1, m_2\}$, we apply a magnetic field $B = 66$ G, which induces a Zeeman shift of the order of several MHz between molecular lines with different M_T projection. In this case the spectrum is complicated by the presence of a plethora of features originated by the Zeeman splitting of different transitions, which makes it difficult to label individual lines. The association of the PA lines to a particular spin flavour has been realized preparing different SU(2) mixtures and acquiring individual spectra for each of them, as it is shown in Fig. S1b. In particular, at this magnetic field, we identify three strong PA lines at 778.3 MHz, 792.8 MHz and 802.0 MHz which are associated to doublons with spin compositions $|12\rangle = \{+5/2, +1/2\}$, $|23\rangle = \{+1/2, -5/2\}$ and $|31\rangle = \{-5/2, +5/2\}$, respectively.

For the measurements reported in Fig. 4 of the main text, $\gamma(12)$ is calculated from a spin-resolved measurement of doublons in the $|12\rangle$ and $|31\rangle$ channels as $\gamma(12) = N_d(12)/(N_d(12) + 2N_d(31))$, taking into account $N_d(23) = N_d(31)$. This assumption is justified by the equal population of the two flavours $|1\rangle$ and $|2\rangle$ after the adiabatic preparation sequence described in Sec. S.V, as shown in Fig. S5.

S.II. DATA ANALYSIS

The number of double occupancies is obtained from a direct measurements of the total number of atoms, with and without photoassociation (PA), obtained through standard time-of-flight absorption imaging (see Sec. S.I). Measurements with and without PA are alternated in time and the number of double occupancies N_d is obtained by the difference between close pairs, in order to compensate for fluctuations in the initial number of atoms N (without PA) due to slow environmental drifts. For the same set of parameters $\{U/D, \Omega/D\}$ we acquire from 40 to 80 (N, N_d) pairs.

The experimental points in Figs. 2 and 4 are obtained by a bootstrapping method in which the raw data are resampled uniformly over a chosen subrange of N, in bins of width $\delta N = 4 \times 10^3$ for Fig. 2a, and over an extended range $N = (5 \dots 35) \times 10^3$ for Fig. 2b,c and Fig. 4. The error bars are obtained as the standard deviation of the mean values for different resamplings of the same N interval.

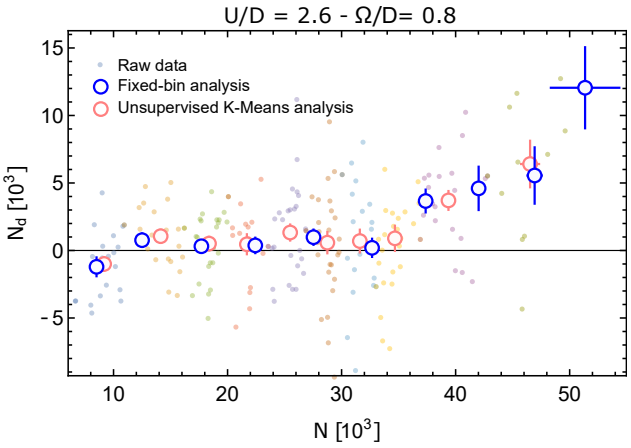

FIG. S2. **Comparison between different data analysis methods.** The number of doublons in the $|12\rangle$ channel is shown as a function of the total atom number N for $U/D = 2.6$ and $\Omega/D = 0.8$, for different data analysis methods. Small points are the raw (N, N_d) data, with different colours representing the clusters of attribution after the application of the unsupervised K-Means method with $K = 10$ groups. Pink points represent the mean values for the different K-Means clusters. Blue points are obtained after the analysis explained in S.II with fixed bin widths.

S.III. UNSUPERVISED MACHINE-LEARNING ANALYSIS

In addition to the data analysis presented in the main text and detailed in S.II, we have performed an additional analysis of the flavour-selective double occupancies, based on an unsupervised machine-learning approach. The raw datasets are large, with at least 200 acquisitions of pairs (N, N_d) for each set of experimental parameters. Following the well-established *K-Means method*[s2], we consider the first component of each pair, i.e. the number of atoms N, and we set (as the only constraint) the number K of groups to divide them into. Once the groups (clusters) are defined, the mean values for both the number of atoms N and the number of doublons N_d for each cluster are evaluated. The error bars are estimated with a bootstrapping procedure.

In Fig. S2 we compare the points obtained with the analysis presented in the main text and those given by the unsupervised K-Means analysis, taking the same number of clusters. The good agreement between them ensures that the specific choice of data analysis procedure does not introduced biases on the results. We note that the K-Means method implies only a constraint on the number of clusters, allowing for a different width among them differently from the main analysis procedure, where the bin size was fixed.

As the datasets for the flavour-selective double occupancies are rather large, we can increase the number of groups K to pinpoint the specific range of atom numbers above which doublons form. The flavour-selective averages obtained with the K-Means analysis are fitted with the piecewise function:

$$N_d = \begin{cases} 0 & N \le N_0 \\ A(N - N_0) & N > N_0 \end{cases} \tag{S.1}$$

where N_0 defines the threshold atom number below which atoms are localised. In Fig. S3 we show the K-Means averages for the coupled flavours $|12\rangle$ and the uncoupled ones $|23\rangle$, together with the results of the fit. The difference between the fitted thresholds for the two doublon flavours $\Delta N_0 = N_0(12) - N_0(23)$ is shown in the inset of Fig. S3 for different values of Ω/D.

This analysis demonstrates that, by increasing the Raman coupling intensity (i.e. lifting the flavour degeneracy more), the threshold for $|12\rangle$ doublons moves to a higher number of atoms, showing an increased localisation in the centre of the trap for the coupled flavours. This result, derived from the unsupervised machine-learning analysis, is consistent with the measurements reported in Fig. 4, and provides another strong indication in support of flavour-selective localization for the symmetry-broken SU(3) Hubbard Hamiltonian.

S.IV. IMPLEMENTATION OF RAMAN COUPLING

The coherent coupling between states $|1\rangle$ $(m = 5/2)$ and $|2\rangle$ $(m = 1/2)$ is realized by exploiting a two-photon σ^+/σ^- Raman transition. The Raman coupling is implemented with two co-propagating $\lambda = 556$ nm laser beams characterized respectively by angular frequencies ω and

$\omega + \delta\omega$. In order to reduce the inelastic photon scattering rate, the two beams are 1.754 GHz blue-detuned with respect to the $^1S_0 \rightarrow {}^3P_1\,(F = 7/2)$ intercombination transition. A 150 G magnetic field is used to define a quantization axis and to remove the degeneracy between the six states of the ^{173}Yb ground-state manifold, which are split according to their nuclear spin m by $207 \times m$ Hz/G.

The σ^+/σ^- coupling between $m = +5/2$ and $m = +1/2$ is obtained by setting the polarization of the two beams to be orthogonal with respect to the quantization axis and adjusting the frequency difference $\delta\omega/2\pi$ in order to compensate the Zeeman splitting and the residual Raman light shift between the two states. As explained in detail in the supplementary material of Ref. S3, this choice for the polarization makes the Raman light shifts largely spin-dependent, thus making the $m = +1/2 \leftrightarrow m = -3/2$ coupling nonresonant and effectively excluding state $m = -3/2$ from the dynamics. For a similar reason, also the $m = -5/2 \leftrightarrow m = -1/2$ coupling is nonresonant and state $|3\rangle$ $(m = -5/2)$ does not participate to the Raman dynamics.

On the basis of the discussion above, the Raman coupling on the basis formed by the three states $\{|1\rangle, |2\rangle, |3\rangle\}$ can be described by the following 3x3 rotating-wave-approximated Hamiltonian

$$\hat{H}_R = \frac{\hbar}{2}\begin{pmatrix} \delta & \Omega & 0 \\ \Omega & -\delta & 0 \\ 0 & 0 & 0 \end{pmatrix} \qquad \text{(S.2)}$$

where Ω is the angular Rabi frequency associated to the Raman coupling and δ is the two-photon detuning with respect to the resonance frequency for the $|1\rangle \leftrightarrow |2\rangle$ transition. No detuning is indicated for state $|3\rangle$ as it is decoupled from the Raman process. In the resonant case $\delta = 0$, $\hat{H}_R$ corresponds to the third term in the many-body Hubbard Hamiltonian in Eq. (1) of the main text.

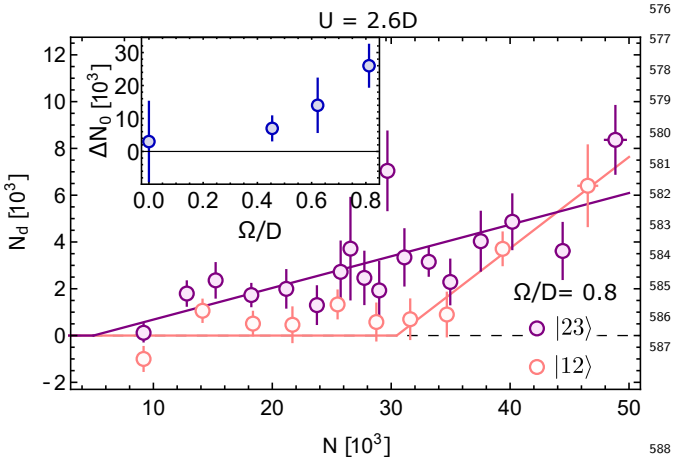

FIG. S3. **Flavour-selective localization.** The number of doublons in different flavour channels is shown as a function of N for $U/D = 2.6$ and $\Omega/D = 0.8$, after a K-Means analysis with $K = 18$ clusters. Pink points show the average number of doublons formed by the coupled flavours $|12\rangle$, while purple points refer to the uncoupled flavours $|23\rangle$. Solid lines are the fits performed with the piecewise function in Eq. S.1. In the inset we show the difference between the fitted thresholds $\Delta N_0 = N_0(12) - N_0(23)$ as a function of the coupling strength Ω.

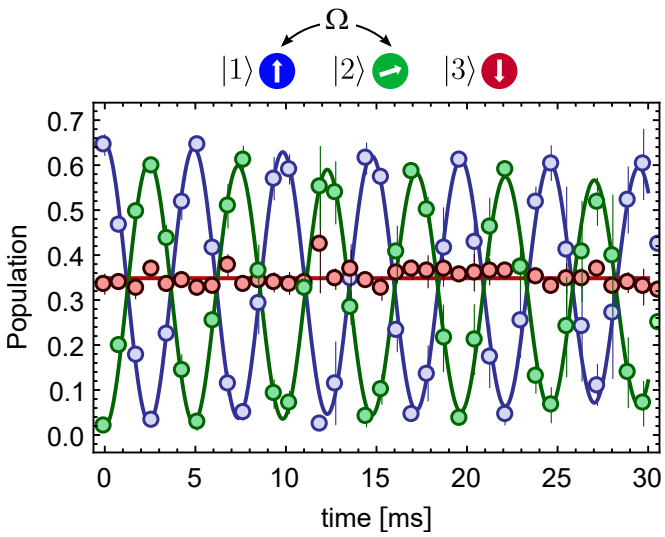

FIG. S4. **Coherent Rabi dynamics.** Population dynamics induced by the sudden activation of a resonant Raman coupling between states $|1\rangle$ and $|2\rangle$ for localized particles in a deep optical lattice (no tunnelling). The points show the fractional population of the states $|1\rangle$ (blue), $|2\rangle$ (green) and $|3\rangle$ (red) as a function of time. The resonant Raman coupling is switched on at time $t = 0$, when the initial fractional populations for the three states are 2/3, 0 and 1/3, respectively (as in the adiabatic state preparation procedure described in Sec. S.V). The solid lines are sinusoidal fits of the experimental data.

The Rabi frequency Ω can be experimentally changed by adjusting the intensities I_1 and I_2 of the two Raman beams, according to the relation $\Omega \propto \sqrt{I_1 I_2}$. In order to assess the value of Ω for given values of the Raman beam intensities I_1 and I_2, we induce resonant Rabi oscillations between states $|1\rangle$ and $|2\rangle$ and determine Ω from a sinusoidal fit of the experimental data, as shown in Fig. S4.

S.V. ADIABATIC STATE PREPARATION

A degenerate Fermi gas of ^{173}Yb atoms, initially confined in a crossed optical dipole trap with harmonic trapping frequencies $\omega_{x,y,z} = 2\pi \times \{55, 96, 73\}$ Hz, is transferred in a simple-cubic 3D optical lattice using a two-step 3s-long adiabatic loading procedure[S4]. The optical lattice is described by a potential energy $V(x, y, z) = V_0\left[\sin^2(\pi x/d) + \sin^2(\pi y/d) + \sin^2(\pi z/d)\right]$, where $d = \lambda/2$ is the lattice spacing and V_0 is the lattice energy depth along each of the three principal axes.

In the first 2 seconds, the lattice intensity is ramped up with a first spline ramp from $V_0 = 0$ to $V_0 = 4E_{rec}$ ($E_{rec} = h^2/8md^2$ is the recoil energy). After this first step, the lattice intensity is further increased with a 1s-long spline ramp to the final value V_0 ranging from $4E_{rec}$ to $15E_{rec}$. During the lattice loading, the depth of the crossed dipole trap is progressively reduced in such a way to keep the harmonic trapping frequencies constant along the three principal axes, independently from the value of V_0.

For the measurements at $\Omega = 0$ the loading procedure described above is applied to a balanced 3-component mixture of ^{173}Yb atoms in the three spin states $|1\rangle$, $|2\rangle$ and $|3\rangle$. The mixture is prepared before the lattice ramp-up procedure with a sequence of optical pumping pulses on the $^1S_0 \rightarrow {}^3P_1$ transition, following the techniques discussed in Ref. 15. The populations of the three spin states are all equal, $N_1 = N_2 = N_3 = N/3$, with experimental imperfections on the order of a few % at most.

For the measurements at $\Omega \neq 0$ the loading procedure starts with a 2-component unbalanced mixture of atoms in states $|1\rangle$ and $|3\rangle$. With a proper choice of optical pumping pulses we adjust the initial populations to be $N_1 = 2N/3$ and $N_3 = N/3$. After the lattice loading, we switch on the Raman beams, initially far detuned from any two-photon transition, and perform an adiatic frequency sweep to bring them resonant with the $|1\rangle \leftrightarrow |2\rangle$ transition. The resonant condition is reached by means of an exponential frequency sweep of the form

$$\delta(t) = \delta_0(e^{-t/\tau} - e^{-T/\tau})/(1 - e^{-T/\tau}) \qquad \text{(S.3)}$$

that reduces the two-photon detuning from $\delta_0 \gg \Omega$ to $\delta = 0$ in a time T and time constant τ (see an example in Fig. S6a). This procedure is an adiabatic passage that brings an atom in state $|1\rangle$ to the lowest-energy dressed state of the Raman-coupled system $|+\rangle = (|1\rangle + |2\rangle)/\sqrt{2}$ (see also the sketch in Fig. 1 of the main text). We note that, due to the initial spin unbalance and because of the equal-weighted admixture of states $|1\rangle$ and $|2\rangle$ in the Raman-dressed states, at the end of the detuning ramp the population is equally distributed among the spins, $N_1 = N_2 = N_3 = N/3$, as it was natively in the loading protocol employed for $\Omega = 0$.

The ramp parameters δ_0, T and τ are chosen according to a numerical analysis in which we solve the time-dependent Schrödinger equation associated to the Raman Hamiltonian in Eq. (S.2), verifying that at the end of the ramp the initial state is effectively projected onto the Hamiltonian lowest energy eigenstate. Experimentally, we check the adiabaticity of this procedure by verifying that the initial unbalanced $|1\rangle$-$|3\rangle$ mixture can be recovered with a reversed detuning ramp following that in Eq. (S.3). To further assess the loading fidelity, we verify the time stability of the spin populations at the end of the loading ramp, as shown in Fig. S5. In both the cases, we measure population differences of a few % at most, validating the effectiveness of this loading procedure.

S.VI. NUMERICAL VALIDATION OF THE LOADING PROCEDURE

In order to assess the validity of the adiabatic state preparation at the many-body level, we have developed a numerical simulation based on the exact diagonalization of Eq. (1) on a reduced-scale version of our system. We consider N three-component fermions in a 1D lattice with N_s sites, retaining all the relevant terms of Eq. (1): hopping, repulsive interactions, Raman coupling between states $|1\rangle$ and $|2\rangle$. We work in the occupation number basis in which the Hilbert space is constituted by the Fock vectors

$$|\psi\rangle = |n_{1,1}, ..., n_{\alpha,i}, ..., n_{3,N_s}\rangle \qquad \text{(S.4)}$$

where $n_{\alpha,n} = \{0, 1\}$ is the occupation number for a particle in internal state $\alpha = \{1, 2, 3\}$ in the lattice site $i = \{1, ..., N_s\}$. In this basis we can write the many-body Hamiltonian as

$$\hat{H} = -t\sum_{i,\alpha}\left(\hat{c}^\dagger_{\alpha,i}\hat{c}_{\alpha,i+1} + \text{h.c.}\right) + U\sum_{i,\alpha,\beta\neq\alpha}\hat{n}_{\alpha i}\hat{n}_{\beta i} + \\ + \frac{\Omega}{2}\sum_i\left(\hat{c}^\dagger_{1,i}\hat{c}_{2,i} + \text{h.c.}\right) + \frac{\delta}{2}\sum_i(\hat{n}_{1,i} - \hat{n}_{2,i}) \qquad \text{(S.5)}$$

where we have added the last term to take into account the detuning of the Raman coupling (already introduced in the rotated-wave-approximated Hamiltonian of Eq. (S.2)), that is crucial in the state preparation protocol.

We simulate the effect of our loading procedure for a system composed by $N = 3$ particles in a lattice with $N_P = 3$ sites. In this case, the dimension of the Hilbert space associated to the system is $\binom{3\,N_S}{N} = 84$. Scaling the

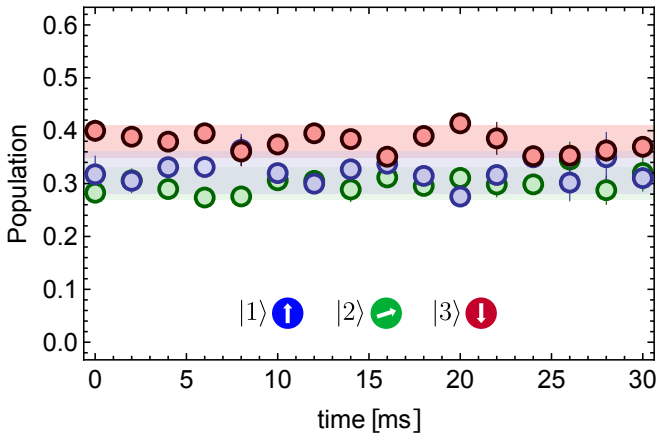

FIG. S5. **State population after adiabatic state preparation**. Fractional state population as a function of time after the adiabatic state preparation sequence. Points are the mean value of 3 independent measurements. Shaded regions represent the standard deviation with respect to the mean value. The slight excess of $|3\rangle$ atoms in this dataset has to be attributed to an imperfect optical pumping before the adiabatic state preparation procedure.

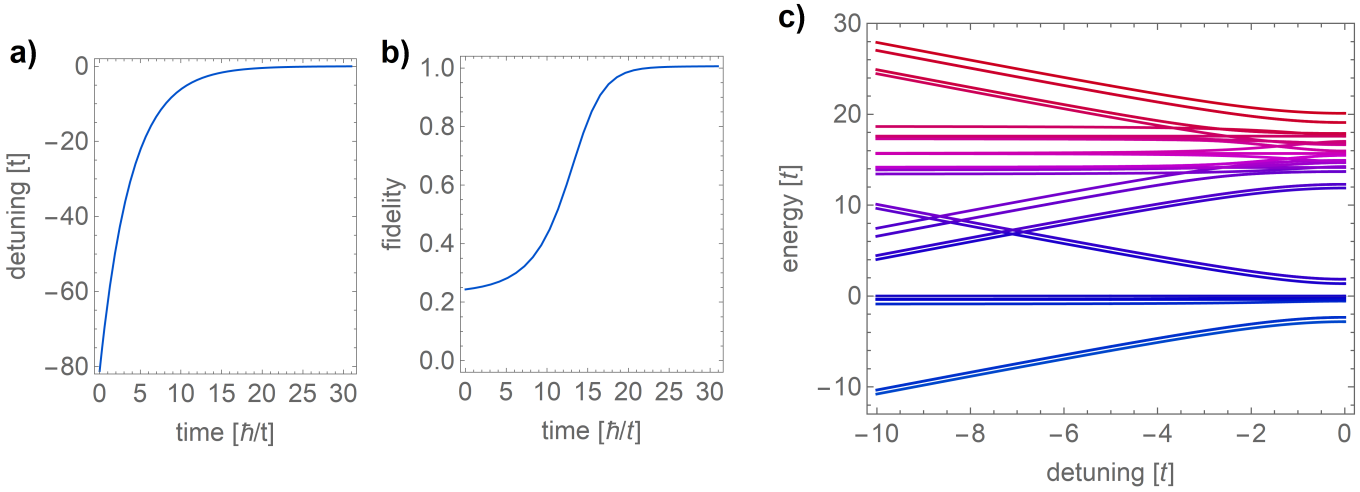

FIG. S6. **Numerical analysis of adiabatic state preparation. a)** Raman detuning ramp used for the preparation of the initial state. The parameters refer to the actual ramp used in the experiment for the preparation of the system for $U = 2.6D$ and $\Omega = 0.35D$. **b)** Calculated fidelity $|\langle\Psi_f|\Psi(t)\rangle|^2$ of the time-evolved state $|\Psi(t)\rangle$ with respect to the target ground state at the end of the ramp $|\Psi_f\rangle$. The calculation has been performed for a small system of 3 particles in 3 sites for $U = 2.6D$, $\Omega = 0.35D$ and the same detuning ramp shown in panel a). **c)** Full spectrum of the system for $U = 2.6D$ and $\Omega = 0.35D$ and different Raman detunings (see text fore more details).

problem to bigger lattices is possible but computationally expensive. In order to simulate the loading scheme with $\Omega \neq 0$, we fix the initial populations to be $\{N_1, N_2, N_3\} = \{2, 0, 1\}$, where N_α refers to the total number of particles in state α. We determine the ground state $|\Psi_0\rangle$ before the Raman loading as the lowest-energy eigenstate of the Hamiltonian in Eq. (S.5), with Ω=0, that is compatible with the constraint on the populations (i.e. $\{2, 0, 1\}$). The Raman loading is then simulated by solving the time-dependent Schrödinger equation in the presence of all the terms of Eq. (S.5), where Ω is kept fixed at the final value and δ is swept from $\delta \gg \Omega$ to $\delta = 0$ according to Eq. (S.3), as discussed in Sec. S.V.

In order to validate the loading procedure we calculate the fidelity between the time-evolved state $|\Psi(t)\rangle = e^{-i\hat{H}t/\hbar}|\Psi_0\rangle$ and the target wavefunction, that is defined as the lowest-energy eigenstate $|\Psi_f\rangle$ of the final Hamiltonian with $\delta = 0$ that is compatible with the constraint on the populations $N_1 + N_2 = 2$ and N_3=1. An example is shown in Fig. S6b for the actual detuning ramp used in the experiment to prepare the state at $U = 2.6D$ and $\Omega = 0.35D$.

Fig. S6c shows the full spectrum of the system as a function of the Raman detuning. There it is evident that the ground state of the system at large detuning $|\Psi_0\rangle$ is adiabatically connected with the ground state $|\Psi_f\rangle$ on resonance. We note that, even if the system initially starts with an unbalanced mixture of two species only, after this procedure it behaves as a mixtures of three species $N_1 = N_2 = N_3 = 1$ all interacting among themselves: in particular, in the presence of tunnelling and interactions between the atoms, the state rotation induced by the detuning sweep does not happen uniformly in all the sites of the lattice, making the atoms initially in state $|1\rangle$ distinguishable and therefore, interacting, at the end of the state preparation sequence.

S.VII. DYNAMICAL MEAN-FIELD THEORY CALCULATIONS

We solve the model in Eq. (1) using Dynamical Mean-Field theory (DMFT)[22], a non-perturbative theoretical method which maps a lattice model onto an effective impurity model. The interaction of the site with the rest of the lattice is approximated by an effective dynamical bath which is determined self-consistently. This allows to fully capture the quantum dynamics while freezing spatial fluctuations beyond mean-field. We solve the model in a Bethe lattice of bandwidth W, which is known to account correctly for the physics of three-dimensional lattices. The impurity model is solved using an exact-diagonalization solver developed at SISSA[S5] which requires to describe the bath in terms of a finite number of levels N_b that we fix to 9 in the calculations reported in this work.

DMFT is naturally formulated in a grandcanonical ensemble, where the total density is fixed by a chemical potential μ and the occupations of the various flavours are not fixed. In order to enforce the experimental population constraint $N_1 + N_2 = 2N_3$ in the presence of the coupling Ω, we have to include an external field which counterbalances the tendency to favour (for total occupation of 1) the occupation of the coupled flavours $|1\rangle$ and $|2\rangle$. Therefore the Hamiltonian is supplemented by the

terms

$$\hat{H}_{fields} = \sum_i \left(-\mu \sum_\alpha \hat{n}_{\alpha i} + h\left(\hat{n}_{1i} + \hat{n}_{2i} - 2\hat{n}_{3i}\right) \right), \tag{S.6}$$

where μ and h have to be determined self-consistently to reach a total occupation of 1 fermion per site. For a uniform infinite lattice, we have drawn a phase diagram based on the flavour-resolved quasiparticle weight Z_α, which is 1 for a non-interacting fermion and it is reduced by the interactions. The global Mott transition is reached when all the Z_α vanish, while a sharp crossover is observed between a standard metal and a region of selective correlation where the quasiparticle weight of the coupled species rapidly drops to a value smaller than 0.05.

Besides the calculations for a uniform lattice, we also have used DMFT to estimate the effect of the harmonic trapping potential

$$\hat{V}_T = \kappa \sum_{i,\alpha} R_i^2 \hat{n}_{\alpha i}, \tag{S.7}$$

where R_i is the distance of the site i from the center of the trap. In order to reduce the computational cost, we have employed a local-density approximation (LDA), which assumes that the local properties of the system can be computed from a uniform model with the local values of the physical parameters, in the present case of the potential given by the harmonic trap. This amounts to have a local value of the chemical potential $\mu' = \mu - \kappa \sum_{i,\alpha} R_i^2$.

In order to build the global observables for the trapped system, we have solved the model given by Eqs. (1) and (S.7) for a wide range of values of μ' spanning the whole range of densities from 0 to 3. For every value of μ' we have found the value of h which gives $N_1 = N_2 = N_3$.

The global observables (total number of particles, doublons, flavour-selective doublons) are then obtained integrating the local counterparts over the whole system. In this way we obtain the plots of doublons as a function of the total number of particles shown in the manuscript.

S.VIII. DENSITY MATRIX RENORMALIZATION GROUP CALCULATIONS

We also solve the model in Eq. (1) by means of a Density Matrix Renormalization Group (DMRG) calculation powered by the ITensor library[S6]. We fix the size of the system as $L = 30$ and the total number of particles as $N = 21$. We simulate the internal states as effective physical sites with the redefinition of proper tunnelling and interaction couplings, which results in a total of $N_L = 90$ lattice sites. We find the ground state of the Hamiltonian in Eq. (1) by performing $35 - 50$ DMRG sweeps, with a maximum bond dimension in the interval $(20, 200)$. To enforce particle number conservation in the Raman-coupled case, we introduce an additional chemical potential defined as the h term in Eq. (S.7). The number of doubly occupied sites shown in Fig. 3 also includes the number of triple occupancies (giving a maximum contribution of $\sim 10\%$ at small values of U, Ω).

[S1] J. H. Han, J. H. Kang, M. Lee, and Y. Shin, Photoassociation spectroscopy of ultracold ^{173}Yb atoms near the intercombination line, Phys. Rev. A **97**, 013401 (2018).

[s2] A. Coates and A. Y. Ng, Learning Feature Representations with K-means, *Neural Networks: Tricks of the Trade* (Springer, 2012).

[S3] M. Mancini, G. Pagano, G. Cappellini, L. Livi, M. Rider, J. Catani, C. Sias, P. Zoller, M. Inguscio, M. Dalmonte, and L. Fallani, Observation of chiral edge states with neutral fermions in synthetic Hall ribbons, Science **349**, 1510 (2015).

[S4] M. Miranda, R. Inoue, N. Tambo, and M. Kozuma, Site-resolved imaging of a bosonic Mott insulator using ytterbium atoms, Phys. Rev. A **96**, 4, 043626 (2017).

[S5] M. Capone, L. de' Medici, and A. Georges, Solving the dynamical mean-field theory at very low temperatures using the Lanczos exact diagonalization, Phys. Rev. B **76**, 245116 (2007).

[S6] ITensor Library (version 3.1) http://itensor.org